

Deep Learning in RF Sub-sampled B-mode Ultrasound Imaging

Yeo Hun Yoon, Shujaat Khan, Jaeyoung Huh, and Jong Chul Ye, *Senior Member, IEEE*

Abstract—In portable, three dimensional, and ultra-fast ultrasound (US) imaging systems, there is an increasing need to reconstruct high quality images from a limited number of RF data from receiver (Rx) or scan-line (SC) sub-sampling. However, due to the severe side lobe artifacts from RF sub-sampling, the standard beamformer often produces blurry images with less contrast that are not suitable for diagnostic purpose. To address this problem, some researchers have studied compressed sensing (CS) to exploit the sparsity of the image or RF data in some domains. However, the existing CS approaches require either hardware changes or computationally expensive algorithms. To overcome these limitations, here we propose a novel deep learning approach that directly interpolates the missing RF data by utilizing redundancy in the Rx-SC plane. In particular, the network design principle derives from a novel interpretation of the deep neural network as a cascaded convolution framelets that learns the data-driven bases for Hankel matrix decomposition. Our extensive experimental results from sub-sampled RF data from a real US system confirmed that the proposed method can effectively reduce the data rate without sacrificing the image quality.

Index Terms—Deep learning, ultrasound imaging, low-rank Hankel matrix, convolutional framelets

I. INTRODUCTION

DUE to the excellent temporal resolution with reasonable image quality and minimal invasiveness, ultrasound imaging has been adopted as a golden-standard for many disease diagnosis in heart, liver, etc. Accordingly, there have been many research efforts to extend the US imaging to new applications such as portable imaging in emergency care [1], 3-D imaging [2], ultra-fast imaging [3], [4], etc. However, the common technical hurdle in these applications is the lack of techniques to reconstruct high resolution images from significantly reduced radio-frequency (RF) data under acquisition physics constraint.

Specifically, according to the Nyquist sampling theorem, the sampling rate for US transducer should be at least four times the central frequency of the emitted pulse [5]. Consequently, to achieve better spatial resolution, high speed analog-to-digital converter (ADC) should be used for receiver (Rx) portion of the US transducer, which is the major part of the power consumption of the transducer. Accordingly, in portable US systems, a small number of Rx elements are used to reduce power consumption, which also reduces the size of the receiver aperture, resulting in deterioration of image quality.

In B-mode imaging, the whole imaging area should be swept using focused RF scan-lines. The acquisition time of an

RF line is determined by the speed of sound, which limits the temporal resolution of B-mode imaging. Therefore, to achieve a higher frame rate in ultra-fast imaging or 3-D US imaging, the number of scan lines should be significantly reduced. This in turn leads to severe downsampling artifacts.

To address these problems, compressed sensing approaches have been investigated [6], [5], [7], [8]. However, computationally expensive optimization algorithms are usually required. Recently, Wagner *et al* [7] models a scan line profile as the finite rate of innovation (FRI), and proposed a specially-designed hardware architecture that enables high resolution scan line reconstruction [7]. Another recent proposal is direct RF interpolation using the low rank Hankel matrix completion approach [9]. In particular, thanks to the strong correlation between RF data across scan lines and adjacent temporal frames, Jin *et al* [10] showed that a rank deficient Hankel structured matrix can be obtained from the reordered RF data. Accordingly, the missing RF data can be estimated using an annihilating filter-based low rank Hankel matrix completion approach (ALPHA) without ever changing hardware structure [9]. However, the algorithm is computationally very expensive, which is not suitable for routine clinical applications.

Therefore, one of the most important contributions of this paper is to show that the Hankel matrix-based low-rank interpolation of RF data can be quickly solved using deep convolutional neural network (CNN). In particular, inspired by recent discovery that a CNN can be interpreted as a *deep convolutional framelets* obtained from a decomposition of the Hankel matrix [11], we construct a CNN that performs direct RF data interpolation. Thus, the final reconstruction can be done using the standard delay-and-sum (DAS) beamformer without changing any hardware/software beamformer structures. Compared to an image domain CNNs that attempts to learn acquisition geometry-dependent artifacts, one of the most important advantages of the proposed RF domain CNN is its generalization power. Specifically, although an image domain deep learning requires many sets of data from different acquisition geometries and body areas [12], our CNN can be trained using RF data that is measured by a specific transducer for a particular organ, but it can be also used for other type of transducers and/or different organs. Therefore, the proposed system is very practical in real applications.

Extensive experimental results using RF data from a real US system confirmed that the proposed method has significant potential for RF sub-sampled B-mode US systems.

The authors are with the Department of Bio and Brain Engineering, Korea Advanced Institute of Science and Technology (KAIST), Daejeon 34141, Republic of Korea (e-mail: {caffemocha, jong.ye}@kaist.ac.kr).

II. THEORY

A. B-mode ultrasound imaging

A B-mode ultrasound imaging, which is most widely used in practice, scans the body using focused beams and displays the 2-D image as shown in Fig. 1. Here, SC, Rx and DAS denote the scan line for each ultrasound beam, receivers of the transducer, and delay-and-sum beamformer, respectively. More specifically, after a focused ultrasound beam is illuminated along the scan line as shown in Fig. 1(a), the ultrasound beam is reflected at some tissue boundaries and the reflected US data are recorded by Rx as RF data (see Fig. 1(b)). Thus, Depth-Rx coordinate RF data is obtained for each scan line (SC), and this is repeated for each scan line to obtain a 3-D cube of RF data in Depth-Rx-SC coordinates. In classical US systems, a transducer has a hardware DAS beamformer that uses the 3-D stacked data to generate a time frame which is then sent to the image station (see Fig. 1(c)). On the other hand, software-based US systems transfer RF data directly via high-speed cable, where a software-based beamformer reconstructs images.

B. RF sub-sampled US systems

Here, we consider two types of proof-of-concept RF sub-sampled US systems. The first one is a randomly sub-sampled dynamic aperture US system [10] that acquires only partial RF data as shown in Fig. 2(a). Because the hardware does not need to be changed, this method can be easily used in any US

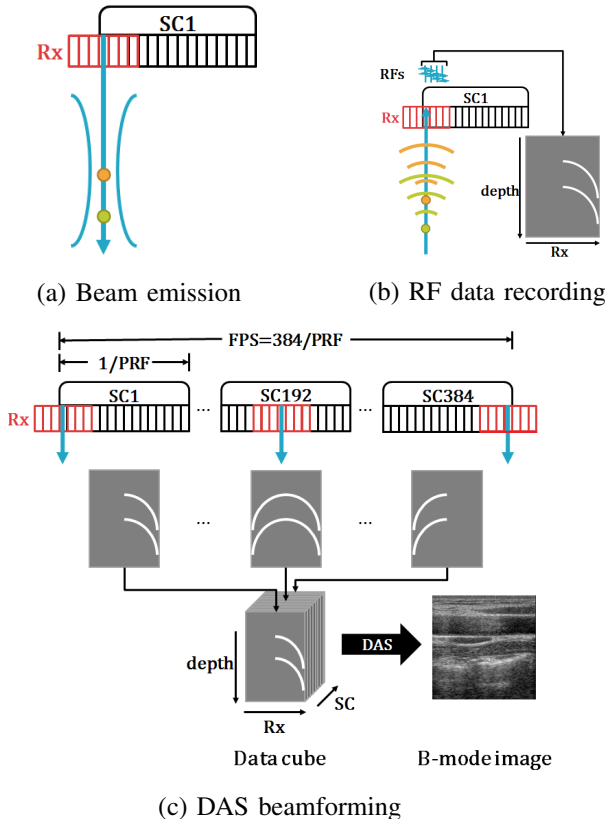


Fig. 1. Imaging flow of the standard B-mode ultrasound imaging. PRF : pulse repetition frequency, FPS : frame per second.

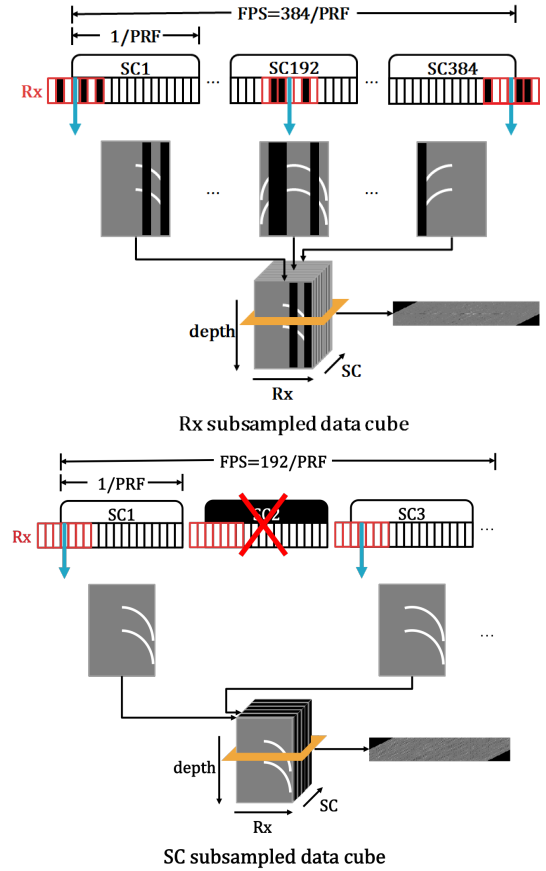


Fig. 2. (Top) Data acquisitions of the randomly sub-sampled dynamic aperture US system. (Bottom) data acquisitions of the SC sub-sampled US system, when downsampling ratio is 2.

system with software beamformer to reduce data transmission bandwidth and power-consumption by minimizing the active Rx number. Moreover, this may be also good for a portable US system which has a smaller number of Rx channels due to the limited transmission bandwidth. The second one is the SC sub-sampled US system as shown in Fig. 2(b). By skipping some scan lines, the frame rate limit can be reduced and a high frame rate can be achieved with 2D or 3D scans. In fact, the SC sub-sampling can be combined with Rx sub-sampling to further reduce the data band-width.

In both scenarios, the main objective is to obtain high quality images using sub-sampled RF data due to limited Rx or SC lines.

C. Redundancy of RF data and low-rank Hankel matrix

Recall that B-mode ultrasound measurements are obtained by point-wise sampling for each scan line. Since the scan line only changes incrementally, the acquired Rx data along the detectors does not change rapidly for each scan line. This implies that some degree of skew redundancy exists in the Rx-SC coordinate data as shown in Fig. 3.

This type of redundancy can be easily seen as a sparsity in the Fourier domain as demonstrated in Fig. 3. Therefore, when the Fourier spectrum of the Rx-SC image is denoted by $\hat{F}(\omega)$,

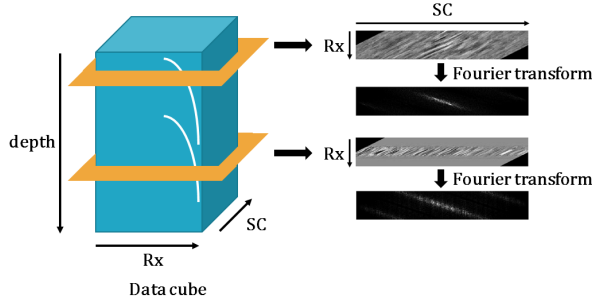


Fig. 3. Rx-SC coordinate data from depth-Rx-SC data cube and its Fourier spectrum.

then we can find a function $\widehat{K}(\omega)$ in the spectral domain such that their multiplication becomes zero:

$$\widehat{F}(\omega)\widehat{K}(\omega) = 0, \quad \forall \omega. \quad (1)$$

This is equivalent to the convolutional relationship in the Rx-SC domain:

$$F \circledast K = 0, \quad (2)$$

where $F \in \mathbb{R}^{n_1 \times n_2}$ denotes the discrete 2-D image and $K \in \mathbb{R}^{d_1 \times d_2}$ is often referred to as the *annihilating filter* [13]. Furthermore, this can be represented in a matrix form :

$$\mathbb{H}_{d_1, d_2}(F) \overline{\text{VEC}(K)} = 0, \quad (3)$$

where $\text{VEC}(K)$ denotes the vectorization operation by stacking the column vectors of the 2-D matrix K and \bar{v} is a flipped version of the vector v . Here, $\mathbb{H}_{d_1, d_2}(F) \in \mathbb{R}^{n_1 n_2 \times d_1 d_2}$ is the *block Hankel matrix* for the image $F = [f_1, \dots, f_{n_2}] \in \mathbb{R}^{n_1 \times n_2}$, which is defined under the periodic boundary condition as follows:

$$\mathbb{H}_{d_1, d_2}(F) = \begin{bmatrix} \mathbb{H}_{d_1}(f_1) & \mathbb{H}_{d_1}(f_2) & \cdots & \mathbb{H}_{d_1}(f_{d_2}) \\ \mathbb{H}_{d_1}(f_2) & \mathbb{H}_{d_1}(f_3) & \cdots & \mathbb{H}_{d_1}(f_{d_2+1}) \\ \vdots & \vdots & \ddots & \vdots \\ \mathbb{H}_{d_1}(f_{n_2}) & \mathbb{H}_{d_1}(f_1) & \cdots & \mathbb{H}_{d_1}(f_{d_2-1}) \end{bmatrix}, \quad (4)$$

and $\mathbb{H}_{d_1}(f_i) \in \mathbb{R}^{n_1 \times d_1}$ is a Hankel matrix:

$$\mathbb{H}_{d_1}(f_i) = \begin{bmatrix} f_i[1] & f_i[2] & \cdots & f_i[d_1] \\ f_i[2] & f_i[3] & \cdots & f_i[d_1 + 1] \\ \vdots & \vdots & \ddots & \vdots \\ f_i[n] & f_i[1] & \cdots & f_i[d_1 - 1] \end{bmatrix}. \quad (5)$$

Eq. (3) implies that the block Hankel matrix constructed from the RF data in Rx-SC domain is rank-deficient. Furthermore, its rank is determined by sparsity level in the spectral domain as theoretically proven in [9]. In fact, Jin *et al* [10] utilized this as well as temporal domain redundancy to interpolate missing RF data using low-rank Hankel matrix completion. However, the main limitation of [10] is its computational complexity, which is prohibitive in real applications. In the following, we will show that the low rank properties of block Hankel matrix can be exploited using the deep convolutional

neural network.

D. Deep Convolutional Framelets

Recently, it was shown that CNN is closely related to Hankel matrix decomposition [11]. Here, we examine this by assuming 1-D signal model for simplicity.

Specifically, let $f = [f[1], \dots, f[n]] \in \mathbb{R}^n$ denotes the signal, and d refers to the annihilating filter length. Then, for a given Hankel matrix $\mathbb{H}_d(f) \in \mathbb{R}^{n \times d}$, let $\Phi = [\phi_1 \cdots \phi_n]$ and $\tilde{\Phi} = [\tilde{\phi}_1 \cdots \tilde{\phi}_n] \in \mathbb{R}^{n \times n}$ (resp. $\Psi = [\psi_1 \cdots \psi_q]$ and $\tilde{\Psi} = [\tilde{\psi}_1 \cdots \tilde{\psi}_q] \in \mathbb{R}^{d \times q}$) denote the frame and its dual frame, respectively, satisfying the frame condition:

$$\begin{aligned} \tilde{\Phi}\Phi^\top &= \sum_{i=1}^n \tilde{\phi}_i \phi_i^\top = I, \\ \Psi\tilde{\Psi}^\top &= \sum_{i=1}^q \psi_i \tilde{\psi}_i^\top = I. \end{aligned} \quad (6)$$

Then, Yin *et al* [14] derived the following *convolution framelet* representation:

$$f = \frac{1}{d} \sum_{i=1}^n \sum_{j=1}^q \langle f, \phi_i \circledast \psi_j \rangle \tilde{\phi}_i \circledast \tilde{\psi}_j, \quad (7)$$

where $\{\phi_i \circledast \psi_j\}$ and $\{\tilde{\phi}_i \circledast \tilde{\psi}_j\}$ constitute the frame bases and its dual, respectively. They further showed that if $\mathbb{H}_d(f)$ is low-ranked, then for given Φ and $\tilde{\Phi}$, the bases Ψ and $\tilde{\Psi}$ can be optimally learned from the data such that the framelet coefficients $\langle f, \phi_i \circledast \psi_j \rangle$ can be sparsified. This means that if a nonlinearity, such as rectified linear unit (ReLU), is added to the framelet coefficients as a shrinkage constraint, then the data driven basis Ψ and $\tilde{\Psi}$ will be learned to have the maximum energy compaction of the framelet coefficients if the underlying Hankel matrix is low-ranked.

Another important clue that links the CNN to the low-rank Hankel matrix completion is given by the following matrix equality:

$$\begin{aligned} \mathbb{H}_d(f) &= \tilde{\Phi}\Phi^\top \mathbb{H}_d(F) \Psi\tilde{\Psi}^\top, \\ &= \tilde{\Phi}C\tilde{\Psi}^\top, \end{aligned} \quad (8)$$

where

$$C := \Phi^\top \mathbb{H}_d(F) \Psi. \quad (9)$$

Specifically, one of the most important contributions in [11] was to reveal that (8) and (9) can be equivalently represented by the decoder and encoder convolution, i.e:

$$f = (\tilde{\Phi}C) \circledast \tau(\tilde{\Psi}), \quad (10)$$

$$C = \Phi^\top (f \circledast \Psi), \quad (11)$$

where

$$\bar{\Psi} := [\bar{\psi}_1 \cdots \bar{\psi}_q] \in \mathbb{R}^{d \times q}, \quad \tau(\tilde{\Psi}) := \frac{1}{d} \begin{bmatrix} \tilde{\psi}_1 \\ \vdots \\ \tilde{\psi}_q \end{bmatrix} \in \mathbb{R}^{dq}.$$

The convolution in (11) is the single-input multi-output (SIMO) convolution, while the convolution in (10) is the multi-input single-output (MISO) convolution. They corresponds to

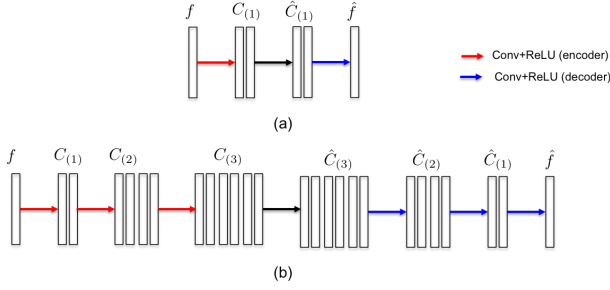


Fig. 4. (a) A single layer encoder-decoder network, and (b) multi-layer encoder-decoder network.

the convolution operations in CNN [11]. More specifically, if $\Phi = I$, then the structure in (11) and (10) is in fact equivalent to one layer of encoder-decoder network as shown in Fig. 4(a). Moreover, a similar decomposition holds for an extended Hankel matrix $\mathbb{H}_{d|p}(Z)$ constructed from an input matrix $Z = [z_1 \cdots z_p] \in \mathbb{R}^{n \times p}$:

$$\mathbb{H}_{d|p}(Z) = [\mathbb{H}_d(z_1) \quad \cdots \quad \mathbb{H}_d(z_p)] , \quad (12)$$

such that

$$\mathbb{H}_{d|p}(Z) = \tilde{\Phi} C \tilde{\Psi}^T \implies Z = (\tilde{\Phi}) \circledast \tau(\tilde{\Psi}), \quad (13)$$

where

$$C = \Phi^T \mathbb{H}_{d|p}(Z) \Psi \implies C = \Phi^T (Z \circledast \bar{\Psi}), \quad (14)$$

and the encoder and decoder filters are defined by

$$\bar{\Psi} := \begin{bmatrix} \bar{\psi}_1^1 & \cdots & \bar{\psi}_q^1 \\ \vdots & \ddots & \vdots \\ \bar{\psi}_1^p & \cdots & \bar{\psi}_q^p \end{bmatrix}, \in \mathbb{R}^{d \times p \times q} \quad (15)$$

$$\tau(\tilde{\Psi}) := \frac{1}{d} \begin{bmatrix} \tilde{\psi}_1^1 & \cdots & \tilde{\psi}_q^1 \\ \vdots & \ddots & \vdots \\ \tilde{\psi}_1^p & \cdots & \tilde{\psi}_q^p \end{bmatrix}, \in \mathbb{R}^{d \times p \times q} \quad (16)$$

The convolutions in (13) and (14) correspond to the multi-input multi-output (MIMO) convolution used in CNN [11]. The simple signal expansion using (11), (10), (14) and (13) is so powerful that a CNN with the encoder-decoder architecture in Fig. 4(b) emerges from them by inserting the pair (14) and (13) between the pair (11) and (10).

In short, because of the redundancy in Rx-SC domain data, the associated Hankel matrix is low-ranked, which allows convolutional filter learning so that resulting convolutional framelet coefficients becomes sparse. This implies that a directly interpolation of Rx-SC domain RF data is feasible using a deep CNN.

III. METHOD

A. Data set

US data in the RF domain were acquired by E-CUBE 12R US system (Alpinion Co., Korea). Real RF data were acquired by a linear array transducer (L3-12H) with the center frequency of 8.48MHz and a convex array transducer (SC1-4H) with the center frequency of 3.2MHz. The sampling

frequencies were 40MHz. The linear transducer is composed of 64 receivers and 384 scanlines, and the convex array transducer is composed of 64 receivers and 256 scanlines. We first acquired RF data from carotid area of nine subjects using a linear array transducer. The size of each Rx-SC planes is 64×384 (# of Rx \times # of SC). 15750 Rx-SC planes of the seven people data sets are randomly selected for generating training data set, and 2250 Rx-SC planes of the another person data sets are randomly selected for generating validation data set. The remaining one person data sets are used as test set.

In addition, we acquired RF data from liver area from one subject using a convex array transducer. This data set was used to verify the generalization power of the algorithm. The size of each Rx-SC planes is 64×256 (# of Rx \times # of SC). In order to use the CNN trained from linear array, we converted the size of Rx-SC planes of the convex array transducer (64×256) to those of the linear array (64×384) as shown in Fig. 5. Here, the SC data around the boundary, i.e. SC 3, 4, 7, 8, \cdots , 255, 256, are duplicated.

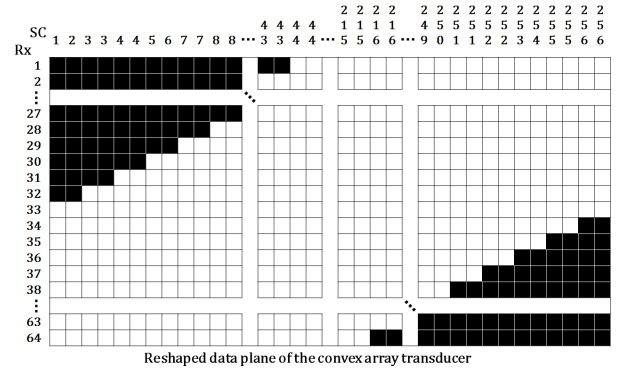


Fig. 5. Reshaping of the convex array transducer (64×256) to the linear array transducer (64×384) using boundary data duplication.

B. RF sub-sampling scheme

As input data, we used randomly sub-sampled data at the downsampling ratio of 4, 8, or 12. In our proposed method that assumes a dynamic aperture US system, the RF data are sub-sampled along the receivers. Since the receiver at the center always obtains the RF data from direct reflection as shown in Fig. 1(c), the receiver has important data. So, we always include RF data from the center receiver.

In the second experiment, the RF data are sub-sampled along the scanlines. Specifically, we consider the sub-sampling in SC-Rx plane. Here, the input data was sub-sampled in two steps. In the first step, the RF data was uniformly sub-sampled along the scanlines with the downsampling ratio of 4 and then in the next step, it was further sub-sampled randomly along the receivers with the downsampling ratio of 4. The overall downsampling ratio for this scheme is $4 \times 4 = 16$.

C. Network Architecture

The proposed CNN is composed of convolution layers, batch normalization layers, ReLU layers and contracting path

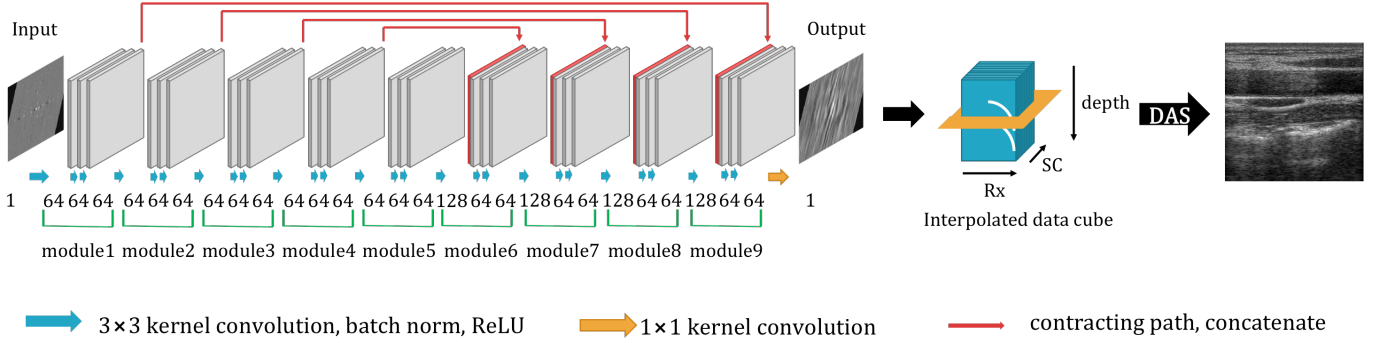


Fig. 6. Our network architecture for RF-interpolation.

with concatenation as shown in Fig. 6. Specifically, the network consists of 28 convolution layers composed of a batch normalization and a ReLU except for the last convolution layer. The first 27 convolution layers use 3×3 kernel, and the last convolution layer uses 1×1 kernel. Four contracting path with concatenation exist. The role of contracting pass in the context of deep convolutional framelets can be found in [11]. As input data, sub-sampled Rx-SC data were used, whereas the full data of Rx-SC plane was used as the label data. If sub-sampling ratio is bigger than 8, additional 3×3 kernel convolution layer, batch normalization layer, and ReLU layer are inserted to each module for enlarge the receptive field size.

The network was implemented with the MatConvNet [15] in MATLAB 2015b environment. For network training, the parameters were estimated by minimizing l_2 norm loss function. And the regularization parameter was 10^{-4} . The network was trained by the stochastic gradient descent. The learning rate started from 10^{-7} and gradually decreased down to 10^{-9} . The weights were initialized using Gaussian random distribution with Xavier method [16]. The number of epoch was 400 for all downsampling rates.

D. Baseline algorithms

For comparative studies, our CNN based interpolation results are compared with the linear interpolation and ALOHA [10]. Specifically, due to the irregular downsampling pattern, the standard linear interpolation algorithm does not work, so we use the grid-based interpolation function `griddata()` in MATLAB. At high sub-sampling ratio (eg. $\times 12$), the Rx-SC plane interpolation using `griddata()` is very inferior, so in this case we use multiple temporal frames together for 3-D interpolation to improve the performance.

ALOHA-based RF interpolation proposed by Jin *et al* [10] further exploits the correlation in temporal direction in addition to the Rx-SC domain redundancy. Specifically, due to strong correlation in the temporal direction, the RF data in Rx-SC domain from adjacent temporal frames shows some level of redundancy and similar patterns as shown in Fig. 7. So, they can be explored by ALOHA [17]. Specifically, we can find the multi-frame annihilating filter relationship [10]:

$$F_i \otimes K_j - F_j \otimes K_i = 0, \quad i \neq j, \quad (17)$$

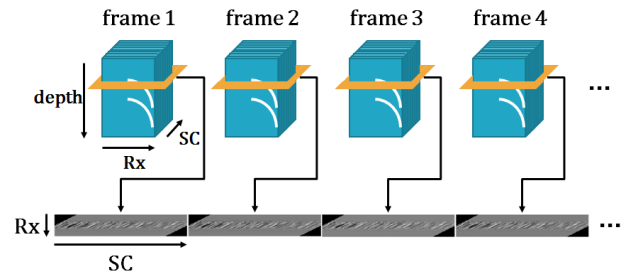


Fig. 7. Spatio-temporal redundancy of Rx-SC coordinate planes. These Rx-SC data are extracted at the same depth.

where F_i denotes the RF data in the Rx-SC data at the i -th frame, and K_i are associated filters. Then, (17) can be represented in a matrix form :

$$\begin{bmatrix} \mathbb{H}_{d_1, d_2}(F_i) & \mathbb{H}_{d_1, d_2}(F_j) \end{bmatrix} \begin{bmatrix} \sqrt{\text{VEC}(K_i)} \\ -\sqrt{\text{VEC}(K_j)} \end{bmatrix} = 0. \quad (18)$$

so that the extended Hankel matrix $\begin{bmatrix} \mathbb{H}_{d_1, d_2}(F_i) & \mathbb{H}_{d_1, d_2}(F_j) \end{bmatrix}$ is rank-deficient. Similarly, we can construct the extended Hankel matrix using RF data from N -time frames:

$$\mathbb{H}_{d_1, d_2 | N}(\{F_i\}_{i=1}^N) := \begin{bmatrix} \mathbb{H}_{d_1, d_2}(F_1) & \cdots & \mathbb{H}_{d_1, d_2}(F_N) \end{bmatrix},$$

and due to the strong spatio-temporal correlation, the extended Hankel matrix still has low rank. Accordingly, the RF interpolation problem can be solved using the following low-rank Hankel matrix completion problem [10]:

$$\begin{aligned} \min_{\{X_i\}_{i=1}^N} & \quad \|\mathbb{H}_{d_1, d_2 | N}(\{X_i\}_{i=1}^N)\|_* \\ \text{subject to} & \quad P_{\Lambda_i} X_i = M_i \end{aligned} \quad (19)$$

where Λ_i denotes the indices of the measured Rx-SC data M_i , P_{Λ_i} denotes the projection to the index Λ_i . The optimization problem (19) can be solved using alternating direction method of multiplier (ADMM) after the matrix factorization [10].

IV. EXPERIMENTAL RESULTS

A. Rx sub-sampling experiments

Fig. 8 compare the results of interpolation, ALOHA and our deep learning method from the Rx sub-sampled data. Our method significantly outperform the other method by eliminating line and blurring artifacts. Then, the trained CNN from

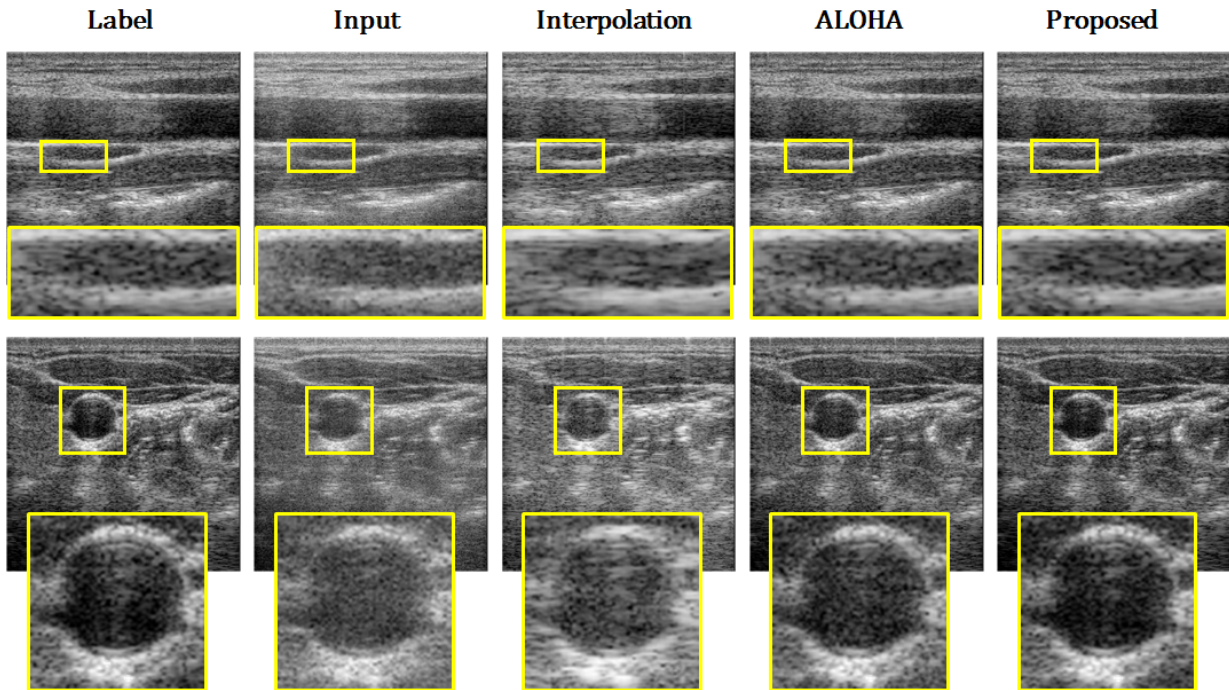


Fig. 8. Linear transducer DAS beamformer reconstruction results from (first column) full RF data, (second column) $\times 12$ downsampled RF data, interpolated RF data using (third column) `griddata()` in MATLAB, (fourth column) ALOHA, and (last column) the proposed CNN-based interpolation, from $\times 12$ sub-sampled RF data.

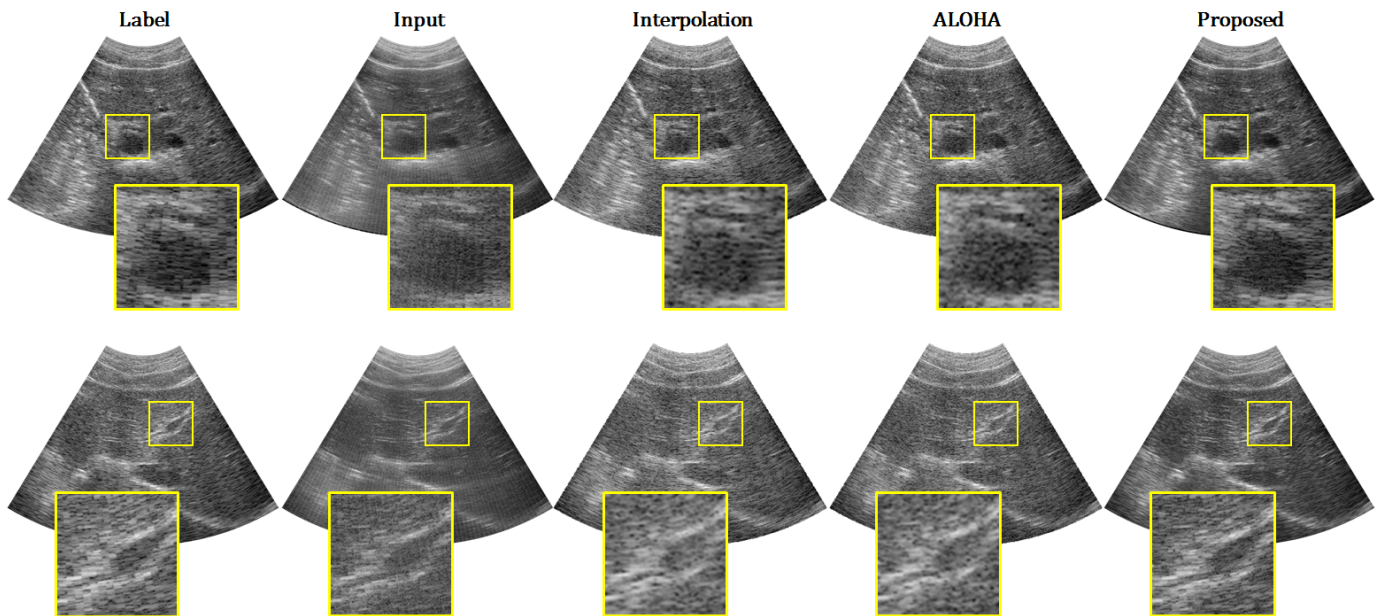


Fig. 9. Convex transducer DAS beamformer reconstruction results from (first column) full RF data, (second column) $\times 12$ downsampled RF data, interpolated RF data using (third column) `griddata()` in MATLAB, (fourth column) ALOHA, and (last column) the proposed CNN-based interpolation, from $\times 12$ sub-sampled RF data.

the linear array transducer was applied to the circular array transducer, and the DAS beamformer output images are shown in Fig. 9. Again, excellent image qualities were observed, which outperformed the existing algorithm significantly. This confirms the generalization capability of our CNN based RF interpolation network.

To quantitatively show the advantages of the proposed deep

learning method, we compared with ALOHA and interpolation methods in terms of the peak-signal-to-noise (PSNR) value and reconstruction time. Fig. 10 and Fig. 11 show PSNR and reconstruction time, respectively. The PSNR value of the proposed deep learning method show 0.7dB improvement compared to ALOHA. For computational time, ALOHA and interpolation reconstructed ten frames simultaneously, so we

compared reconstruction time for ten frames. Fig. 11 confirmed that the reconstruction time of the proposed deep learning method was significantly lower than the ALOHA and interpolation.

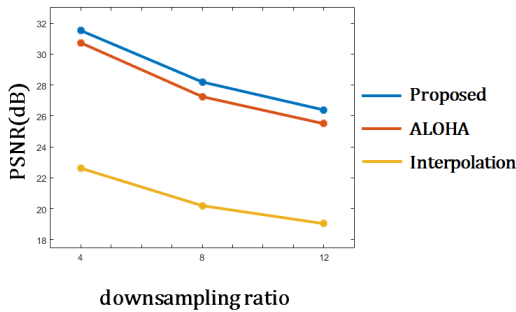


Fig. 10. PSNR with respect to each downsampling ratio. Blue line : our method, Red line : ALOHA-based RF interpolation, Yellow line : MATLAB griddata() RF interpolation.

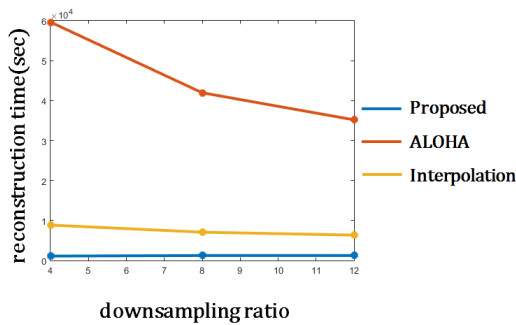


Fig. 11. Reconstruction time with respect to each downsampling ratio. Blue line : our method, Red line : ALOHA-based RF interpolation, Yellow line : MATLAB griddata() RF interpolation.

Fig. 12 showed the validation curve with respect to each training epoch. The algorithm stably converges regardless of the different sub-sampling factor, which proves the robustness of the algorithm.

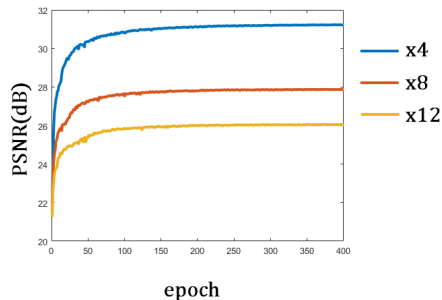


Fig. 12. PSNR with respect to each epoch. Blue line : PSNR of learning at 4x down-sampling ratio, Red line : PSNR of learning at 8x down-sampling ratio, Yellow line : PSNR of learning at 12x down-sampling ratio.

Fig. 13 illustrate representative examples of Rx-SC coordinate data from the linear transducer, and Fig. 14 shows the corresponding B-mode ultrasound images, when Rx down-sampling ratio is 12. The proposed CNN-based interpolation successfully reconstructed the missing RF data from only

7.7% of RF data such that the beamformer removes the blurring artifacts and generates near artifact-free images even in complicated structures. The average of PSNR for the reconstruction B-mode image (x12) is around 26.65dB, which is about 7dB improvement compared to the B-mode images from sub-sampled RF data.

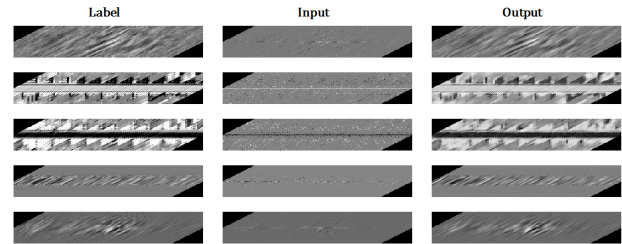


Fig. 13. (first column) full RF data, (second column) x12 sub-sampled RF data, (third column) proposed CNN-based interpolation from x12 sub-sampled RF data.

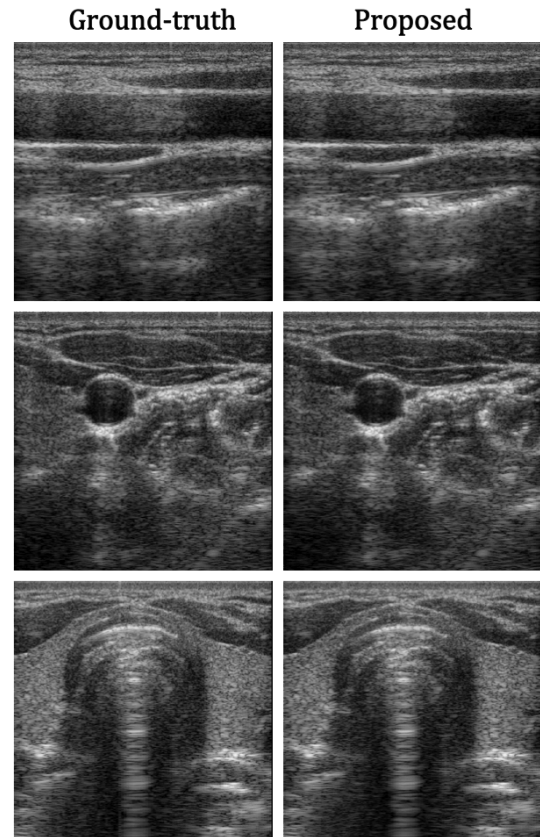


Fig. 14. Linear transducer DAS beamformer images from (first column) full RF data and (second column) the proposed CNN-based RF interpolation from x12 sub-sampled RF data.

Additional reconstruction results from the convex array transducer at x12 Rx sub-sampling are shown in Fig. 15. While the network was trained using linear array transducers, the Rx-SC data of linear array transducer and convex array transducer are similar, so the DAS beamformer provided very accurate reconstruction results without any line artifacts or blurring. It is also remarkable that the accurate reconstruction

was obtained for the liver region, which was never seen by the network trained using the linear array transducer data. The results confirmed the generalization power of the algorithm.

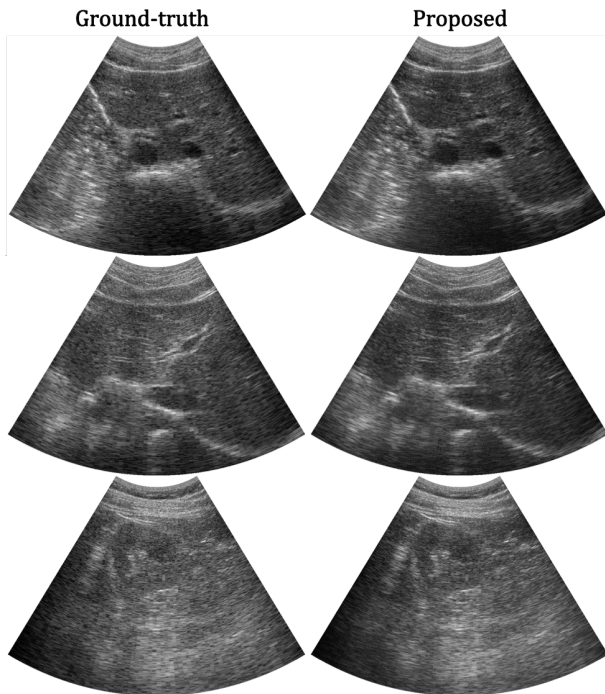


Fig. 15. Convex array transducer DAS beamformer images from (first column) full RF data and (second column) the proposed CNN-based RF interpolation from x12 sub-sampled RF data.

B. SC line sub-sampling experiments

The B-mode images of the linear transducer, reconstructed from the actual, SC-Rx sub-sampled, and CNN-based interpolated RF data are compared in Fig. 16. Here, the SC-Rx sub-sampling factors were 4 and 4, respectively, resulting in net x16 sub-sampling. Due to the SC sub-sampling, the direct beamforming results suffered from severe line artifacts. Using the proposed CNN-based method, the sub-sampled RF-data is drastically improved. This improvement can easily be noticed in the reconstruction results. The CNN-based interpolation eliminates the line artifacts and remarkably recovers the missing information of the image. For the linear array, the average PSNR value of the CNN-based reconstruction B-mode images is 20.20dB, which is about 12.73dB improved compared to the B-mode images from the sub-sampled RF data. To show the generalization power, the training was performed for the SC-Rx sub-sampled linear array RF data, and the same network was used for the interpolation of convex array transducer RF data. For the convex array transducer data, the DAS beamformer output images, reconstructed from the actual, sub-sampled, and CNN-based interpolated RF data are also shown in Fig. 16. Here, again the excellent results are obtained for the unseen convex array data. For the convex array, the average PSNR value of the CNN-based reconstruction B-mode images is 22.82dB, which is about 11.37dB improved compared to the B-mode images from the sub-sampled RF

data. It is noteworthy that from only 6.25% RF-data, the proposed method can efficaciously interpolates the SC-Rx sub-sampled data. Our CNN-based interpolation method shows impressive results in the reconstruction of B-mode images and has the potential to be used for ultrafast or 3-D ultrasound imaging systems.

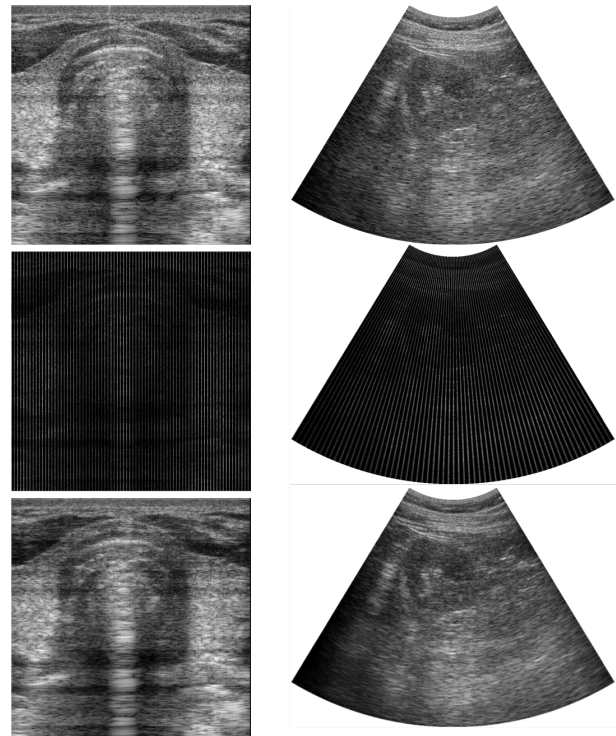


Fig. 16. Reconstruction from SC-Rx sub-sampling RF data (4x4 sub-sampling) for linear and convex array transducers. DAS beamformer reconstruction results from (first row) full data, and (second row) sub-sampled data, and (third row) the proposed CNN results from sub-sampled data.

V. CONCLUSIONS

In this paper, we proposed a novel deep learning approach for accelerated B-mode ultrasound imaging. To exploit the redundancy in the RF domain, the proposed CNN was applied to Rx-SC domain. In contrast to the existing approaches that require hardware changes or computational expensive algorithms, the proposed method does not need any hardware change and can be applied to any B-mode ultrasound system or any transducer. In addition, compared with conventional reconstruction method, PSNR and reconstruction times were significantly improved. Therefore, this method can be an important platform for RF sub-sampled US imaging.

VI. ACKNOWLEDGEMENT

This work is supported by National Research Foundation of Korea, Grant number NRF-2016R1A2B3008104.

REFERENCES

- [1] B. P. Nelson and K. Chason, "Use of ultrasound by emergency medical services: a review," *International journal of emergency medicine*, vol. 1, no. 4, pp. 253–259, 2008.

- [2] G. R. Lockwood, J. R. Talman, and S. S. Brunke, "Real-time 3-D ultrasound imaging using sparse synthetic aperture beamforming," *IEEE Trans. Ultrason., Ferroelect., Freq. Control*, vol. 45, no. 4, pp. 980–988, 1998.
- [3] E. Macé, G. Montaldo, I. Cohen, M. Baulac, M. Fink, and M. Tanter, "Functional ultrasound imaging of the brain," *Nature methods*, vol. 8, no. 8, pp. 662–664, 2011.
- [4] M. Tanter and M. Fink, "Ultrafast imaging in biomedical ultrasound," *IEEE transactions on ultrasonics, ferroelectrics, and frequency control*, vol. 61, no. 1, pp. 102–119, 2014.
- [5] O. Lorintiu, H. Liebgott, M. Alessandrini, O. Bernard, and D. Friboulet, "Compressed sensing reconstruction of 3d ultrasound data using dictionary learning and line-wise subsampling," *IEEE transactions on medical imaging*, vol. 34, no. 12, pp. 2467–2477, 2015.
- [6] H. Liebgott, R. Prost, and D. Friboulet, "Pre-beamformed RF signal reconstruction in medical ultrasound using compressive sensing," *Ultrasonics*, 2012.
- [7] N. Wagner, Y. C. Eldar, and Z. Friedman, "Compressed beamforming in ultrasound imaging," *IEEE Trans. Signal Process.*, vol. 60, no. 9, pp. 4643–4657, 2012.
- [8] C. Quinsac, A. Basarab, D. Kouamé, and J.-M. Grégoire, "3D compressed sensing ultrasound imaging," in *Ultrasonics Symposium (IUS), 2010 IEEE*. IEEE, 2010, pp. 363–366.
- [9] J. C. Ye, J. M. Kim, K. H. Jin, and K. Lee, "Compressive sampling using annihilating filter-based low-rank interpolation," *IEEE Transactions on Information Theory*, vol. 63, no. 2, pp. 777–801, Feb. 2017.
- [10] K. H. Jin, Y. S. Han, and J. C. Ye, "Compressive dynamic aperture b-mode ultrasound imaging using annihilating filter-based low-rank interpolation," in *2016 IEEE 13th International Symposium on Biomedical Imaging (ISBI)*. IEEE, 2016, pp. 1009–1012.
- [11] J. C. Ye and Y. S. Han, "Deep convolutional framelets: A general deep learning framework for inverse problems," *arXiv preprint arXiv:1707.00372*, 2017.
- [12] E. Kang, J. Min, and J. C. Ye, "A deep convolutional neural network using directional wavelets for low-dose x-ray ct reconstruction," *Medical Physics*, vol. 44, no. 10, 2017.
- [13] M. Vetterli, P. Marziliano, and T. Blu, "Sampling signals with finite rate of innovation," *IEEE Trans. Signal Process.*, vol. 50, no. 6, pp. 1417–1428, 2002.
- [14] R. Yin, T. Gao, Y. M. Lu, and I. Daubechies, "A tale of two bases: Local-nonlocal regularization on image patches with convolution framelets," *SIAM Journal on Imaging Sciences*, vol. 10, no. 2, pp. 711–750, 2017.
- [15] A. Vedaldi and K. Lenc, "Matconvnet: Convolutional neural networks for matlab," in *Proceedings of the 23rd ACM international conference on Multimedia*. ACM, 2015, pp. 689–692.
- [16] X. Glorot and Y. Bengio, "Understanding the difficulty of training deep feedforward neural networks," in *Proceedings of the Thirteenth International Conference on Artificial Intelligence and Statistics*, 2010, pp. 249–256.
- [17] K. H. Jin, D. Lee, and J. C. Ye, "A general framework for compressed sensing and parallel mri using annihilating filter based low-rank hankel matrix," *IEEE Transactions on Computational Imaging*, vol. 2, no. 4, pp. 480–495, 2016.